RESEARCH ARTICLE | DECEMBER 27 2024

Sub-ablation-threshold light-induced modification of thin ruthenium layers detected using optical reflectance

Ester Abram ✉ ⓘ ; Nikolai Orlov ⓘ ; Erik C. Garnett ⓘ ; Paul Planken ⓘ

Check for updates

View Online   Export Citation

Articles You May Be Interested In

A nanovolcano array

Physics Today (May 2018)

Thermal atomic layer deposition of ruthenium metal thin films using nonoxidative coreactants

J. Vac. Sci. Technol. A (December 2019)

Direct laser patterning of ruthenium below the optical diffraction limit

Appl. Phys. Lett. (April 2024)

Sub-ablation-threshold light-induced modification of thin ruthenium layers detected using optical reflectance

Ester Abram,[1,2,a)] Nikolai Orlov,[3] Erik C. Garnett,[2,3] and Paul Planken[1,2]

AFFILIATIONS

[1]Advanced Research Center for Nanolithography (ARCNL), Science Park 106, Amsterdam 1098 XG, The Netherlands
[2]Van der Waals-Zeeman Institute, University of Amsterdam, Science Park 904, Amsterdam 1098 XH, The Netherlands
[3]Center for Nanophotonics, AMOLF, Science Park 104, Amsterdam 1098 XG, The Netherlands

[a)]Author to whom correspondence should be addressed: E.Abram@arcnl.nl

ABSTRACT

In semiconductor device manufacturing, wafer materials may be exposed to intense light sources by optical metrology tools. The desired light fluence often needs to be maximized to levels just below the optical damage threshold of materials deposited on the wafer, such as ruthenium. We, therefore, investigate light-induced permanent structural changes to thin Ru films after exposure to single 400 nm wavelength femtosecond pulses in the fluence regime before catastrophic damage. For fluences below that where full-ablation occurs, small optical increases in the reflectivity of up to 4% are observed in the aftermath with a weak probe beam. In this fluence regime, dark-field, scanning electron, and atomic force microscopy images reveal morphological changes such as *top-level ablation*, where only the top part of the ruthenium layer is ablated whereas the lower part still remains on the substrate, and nanovolcano formation. However, neither top-level ablation nor nanovolcano formation is responsible for the reflection increase. Instead, Electron Backscatter Diffraction reveals that in this low fluence regime where reflectivity increases, Ru grains melt and resolidify into larger grains, which is likely responsible for the observed reflectivity increases. This result is reminiscent of our earlier work on aluminum layers and it suggests that there may be more metals that display this behavior.

I. INTRODUCTION

In semiconductor device manufacturing, new technological challenges arise as device structures become smaller and smaller.[1,2] For example, the resistivity of copper and tungsten increases when the dimensions of conducting lines become smaller.[3–5] Ruthenium (Ru) has appeared as a suitable alternative to copper and tungsten because of its good nanoscale conductivity.[6,7] However, in semiconductor device manufacturing, deposited materials must also be able to withstand high optical fluences used by optical metrology tools, for example for wafer alignment in nanolithography machines.

For wafer alignment, diffraction signals from alignment markers, often buried under various deposited, partially opaque materials, are used to determine the absolute position of the wafer.[8,9] For this, visible/NIR light beams, having a Gaussian beam profile,

are often used with wavelengths in the range from about 400 to 1100 nm. For proper wafer alignment, a sufficient amount of diffracted light from the buried alignment markers is required to accurately determine the wafer position. In recent years, however, there has been a clear trend toward making alignment markers smaller and smaller which, for the same incident fluence, would reduce the amount of diffracted light. Therefore, to keep the amount of diffracted light the same, a further increase in the incident light fluence is required, thereby reaching levels where optical damage becomes a possibility. Of particular importance, therefore, is the optical fluence regime around the optical damage threshold. Subtle, light-induced changes that may affect the conductivity of the Ru, can already occur at fluence levels below the threshold for catastrophic damage and should be avoided at all costs. It is, therefore, of critical importance to study light-induced changes to nanometer thick Ru films.

On ruthenium, extensive light-induced damage studies have been performed in the EUV/hard x-ray range.[10–12] Interestingly, it was reported[11] that the absorbed energy spatial distribution in this wavelength regime is similar to that formed by visible light, resulting in a similar thermo-mechanical response. Additionally, using near IR excitation, ablation processes such as crater formation, a fine pattern of dense cracking (craquelure[13]), and top-level ablation[14] in the film after illumination were modeled and measured.[12] In *top-level ablation*, only the top part of the ruthenium layer is ablated whereas the lower part still remains on the substrate, whereas in *full-ablation*, the substrate is exposed due to the removal of the entire layer. These studies, however, focused mostly on fluence levels above the full-ablation threshold, whereas it is likely that subtle material changes can also occur at fluence levels *below* the full-ablation threshold.

In this study, we have looked at what happens when Ru thin films of 8 to 40 nm thick that are exposed to single laser pulses with optical fluences above and below the threshold value for catastrophic damage. At high fluences, catastrophic damage in the form of crater formation, top-level ablation, and the formation of cracks in the Ru are seen, confirming earlier results.[12,14] Within the area exposed by the pump pulse, scanning electron microscopy (SEM) images and atomic force microscopy (AFM) however, reveal the existence of round *nanovolcanoes* with diameters ranging from 50 to 500 nm. These structures appear to have been formed by molten Ru that has locally been pushed outward and has overflowed the surrounding area. AFM measurements also show that at the bottom of the volcanic crater, the glass surface is exposed and appears to be undamaged. Measurements on samples with the Ru layer deposited on scratched substrates show that nanovolcanoes are mostly located along the scratch lines. This suggests that on nominally flat surfaces, stochastic variations in surface roughness increase the chance of nucleation and may therefore be responsible for the random positions of the nanovolcanoes on the substrate.

Interestingly, *below* the threshold fluence for catastrophic damage, small 0.1%–4% pump-induced increases in the optical reflectivity are observed. Electron Backscatter Diffraction (EBSD) measurements indicate that in a fluence regime below that where catastrophic damage occurs, Ru grains have melted and resolidified into bigger grains. In this fluence regime, a small increase in reflectivity is observed, similar to what was measured for aluminum thin films.[15] This suggests that this effect may perhaps be more universal than original thought and could serve as an indication of impending catastrophic optical damage for a wider range of metals.

II. EXPERIMENTAL DETAILS

A. Sample fabrication

Eight to 40 nm thick ruthenium (Ru) layers are deposited by Magnetron Sputter Physical Vapor Deposition (Polyteknik Flextura M506 S) on 0.5 mm thick borosilicate glass substrates, which have been cleaned in a base Piranha solution. Borosilicate glass[16] is chosen because of the negligible absorption at optical wavelengths of 400 and 800 nm. To study the dependence of the substrate, also sapphire, CaF$_2$ and silicon substrates were used. An overview of the samples used in the experiments is shown in Sec. I of the supplementary material. Additionally, relevant ruthenium and

TABLE I. Optical and thermal mechanical properties of ruthenium and ruthenium oxide.

|	Ru	RuO$_2$
$n + ik$ @ 400 nm	2.40 + 4.64i[a]	
$n + ik$ @ 400 nm ellipsometry	2.60 + 5.04i	3.30 + 0.16i
$n + ik$ @ 800 nm	5.04 + 3.94i[a]	
$n + ik$ @ 800 nm ellipsometry	5.51 + 5.10i	2.64 + 0.028i
Melting point T_m (K)	2606[b]	
Boiling point T_b (K)	4420[b]	
Thickness (nm)	8–40	0.5 (native oxide)
Thermal conductivity κ (Wm^{-1}K^{-1})	117[b]	
Specific heat C_l (10^6 Jm^{-3}K^{-1})	2.88[b]	

[a]Reference 17 (pp. 256–261).
[b]Reference 18 (pp. 12–218).

ruthenium oxide properties and used layer thicknesses are given in Table I.

B. Setup

The pump–probe laser setup used for the experiments is shown schematically in Fig. 1 and is explained in more detail in Ref. 15. All experiments presented here are performed in ambient atmosphere.

A Ti:Sapphire oscillator-amplifier combination generates 45−fs laser pulses with a central wavelength of 800 nm at a repetition rate of 1 kHz. In the setup, the beam is split into a weak 800 nm probe beam, and a strong pump beam that is frequency-
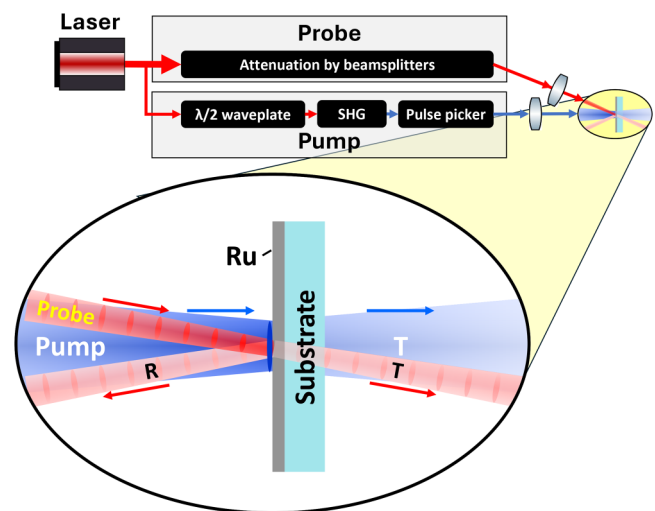
FIG. 1. Schematic of the pump–probe laser setup used for the experiments (top) and the geometry of the beams and the sample (bottom). A detailed description of the entire setup can be found in Ref. 15.

doubled by a Beta Barium Borate (BBO) crystal to 400 nm (type 1 second harmonic generation). Next, a pulse picker system, formed by a 10% duty-cycle chopper and a galvo mirror, selects a single pump pulse. The pump beam is focused using a $f = 20$ cm lens and the sample is placed a short distance before the focal point. The pump is at normal incidence on the sample and the probe beam is at an angle of $\approx 10°$ with respect to the surface normal. Before it is focused onto the sample, the probe beam is reflected off a set of beamsplitters to attenuate the power by a factor of $\approx 10^{-4}$ to a pulse energy $\approx 0.1\,\mu$J. The pump-pulse energy can be varied by rotating the $\lambda/2$-plate which is placed before the BBO. The probe and pump are focused onto the sample to spot sizes of ≈ 15 and $\approx 75\,\mu$m respectively. The geometry of the beams and the sample is schematically shown in Fig. 1. Here, R and T indicate the reflected and transmitted beams. The laser beams used in these experiments have Gaussian beam profiles (see Sec. II A of the supplementary material). Whereas it is not uncommon to use flat-top beam profiles in laser damage experiments,[19,20] Gaussian beam profiles are typically used in metrology tools for wafer alignment. Our experiments are thus closer to the actual use cases. A detailed description of the entire setup can be found in Ref. 15.

Before each measurement series, a Gentec-EO Beamage-4M beam profiler is placed at the sample position, where the pump and probe beam spatially overlap, to measure the pump and probe beam spatial profiles. Furthermore, a Coherent thermopile power sensor is placed in the pump beam path after the last mirror before the focusing lens. This is to calibrate the reference photodetector in order to convert the detector signal into a pump fluence.

In a typical experimental cycle, single pump pulses hit the sample in a six-by-six grid where each subsequent pump shot has a slightly higher fluence. Here, the fluence ranges from well below any measurable morphological or optical change to above the threshold for crater formation. Each site in the six-by-six grid is hit by only one pump pulse. To check reproducibility, each such cycle is repeated several times, leading to the formation of multiple grids. Before each measurement series, the probe alignment with respect to the pump is optimized by maximizing/minimizing the measured power of the probe transmission/reflection after creating a small ablation site by the pump. The same is done after the measurement series to check if no beam drifting occurred and to confirm that the sample and sample stage were aligned properly (see Sec. II B of the supplementary material). At each illuminated site, before pump excitation, the 800 nm reflectivity (R_{pre}) is obtained by measuring the probe reflection and a reference signal using photodetectors. R_{pre} is averaged over a thousand shots giving $\bar{R}_{\text{pre}}$, which enhances the detection sensitivity. The same is done for a thousand probe shots, measured well after pump excitation (>1 ms), when all transient effects have disappeared, giving the average $\bar{R}_{\text{post}}$. The relative difference between $\bar{R}_{\text{pre}}$ and $\bar{R}_{\text{post}}$ normalized to $\bar{R}_{\text{pre}}$ is the *relative reflection change* ΔR,

$$\Delta R(F) = \frac{\bar{R}_{\text{post}}(F) - \bar{R}_{\text{pre}}}{\bar{R}_{\text{pre}}}. \tag{1}$$

These values for ΔR depend on the pump fluence F and are obtained for all ruthenium layers. They are presented in Sec. III.

C. Post-processing

After each measurement series, the sample is taken out of the laser setup for the inspection of the illuminated sites. Each grid containing 36 illuminated sites is inspected by differential interference contrast (DIC/Nomarski) and dark-field (DF) microscopy. Hereafter, a Helios Nanolab 600 scanning electron microscope (SEM) is used to study possible morphological changes. Selected sites are inspected further with a Bruker Dimension Icon atomic force microscope (AFM). For some sites, energy-dispersive x-ray spectroscopy (EDX), to obtain the spatial distribution/concentration of the elements (Ru and O) present in the layer and/or Electron Backscatter Diffraction (EBSD) is used to map the crystal orientation and structure and to obtain grain sizes. EBSD was performed in a Thermo Fisher Scientific Verios 460 SEM using an EDAX Clarity direct detector. The patterns were collected using EDAX APEX software, a 100 pA beam current, 7 kV accelerating voltage, and a 15–200 ms pixel integration time. The patterns were processed in the EDAX OIM software. All obtained patterns were indexed using the Spherical Indexing (SI) approach with Neighbor Pattern Averaging and Reindexing (NPAR) with the Ru phase ($P6_3/mmc$ space group).

For an (elliptical) Gaussian pump beam, where the intensity distribution is Gaussian having a different width in the two orthogonal directions of the ellipse, the local fluence profile, $F(x, y)$, varies with position. In this profile, lines of constant fluence ($F = const.$) take the shape of ellipses. These ellipses correspond to lines where the energy per unit area has a constant value. When a damage mechanism is bounded by a certain threshold fluence F_{th}, the area A bounded by this ellipse equals the area spanned by that damage mechanism. Therefore, for Gaussian beam profiles[21] with a peak fluence of F_0 at its center, A and $\ln(F_0)$ follow the linear relation as expressed in Eq. (2),

$$A = a \ln(F_0) + b. \tag{2}$$

Since the onset of damage occurs at $A = 0$, where $F_0 = F_{\text{th}}$, F_{th} as well as the FWHM of the Gaussian beam waist d_x (long axis) and d_y (short axis) can be expressed in the linear parameters a and b as defined in Eq. (2),

$$F_{\text{th}} = \exp\left(-\frac{b}{a}\right), \qquad d_x = \sqrt{\frac{4\ln(2)a}{\pi\sqrt{1-e^2}}},$$

$$d_y = d_x\sqrt{1-e^2} \qquad \text{with} \qquad d \equiv \sqrt{d_x d_y}, \tag{3}$$

with e being the eccentricity of the elliptical beam profile, which is directly measured ($e \approx 0.70$). Here, a and b are determined from the linear fit to the measurement data of area A vs $\ln(F_0)$ in the so-called Liu-plot.[15,21] A more detailed derivation of Eqs. (2) and (3) can be found in Ref. 22 (pp. 2–3). Since lateral heat diffusion can be neglected here (see Sec. IV B of the supplementary material) and we consider metals here, damage occurs where $F_{\text{local}} > F_{\text{th}}$. By using a Gaussian, instead of a flat-op beam profile,[19,20] F_{th} can be obtained with a high accuracy because of the relation between the damaged area A and the peak fluence F_0 [see Eq. (2)].

III. RESULTS AND DISCUSSION

A. Nanovolcano formation and top-level ablation

We used six samples with nominal ruthenium layer thicknesses of 8, 10, 15, 20, 25, and 40 nm on borosilicate glass substrates.[23] Each sample is illuminated by single-shot 400 nm pulses of different fluences and probed by weak 800 nm pulses. The relative reflection change, ΔR [see Eq. (1)], is measured. These ΔR values are plotted vs peak pump fluence F_0 and are shown in Fig. 2. For low fluences, $\Delta R = 0$ because the pump fluence is too low to permanently change the ruthenium layers. For high enough fluences, ruthenium is removed. Since the transmission of the probe light is higher without the ruthenium layer present, this *full-ablation* will always cause a decrease in ΔR (see Fig. 8 in the supplementary material). In between these low and high fluence regimes, for the 8 and 10 nm ruthenium layer [Figs. 2(a) and 2(b)], there is a small increase in the reflectivity ($\Delta R > 0$). This is slightly different for the 15 to 40 nm thick (nominal) ruthenium layers [Figs. 2(c)–2(f)]. Although there the reflectivity increase is present as well, additional, fairly abrupt changes in the slope of $\Delta R(F)$ are also observed. Each abrupt change may be located at a fluence threshold corresponding to a different damage mechanism. The same figure is shown in part of Fig. 7 of the supplementary material, which includes all found damage mechanisms.

Using SEM and optical microscopy, images of all illuminated sites have been obtained. Different damage mechanisms such as cracking, nanovolcano growth, and top-level ablation of the layer were observed below the threshold fluences for full-ablation. With top-level ablation, roughly the top half of the layer of ruthenium has ablated from the lower half, and the lower part is still intact and remains on the substrate. This is due to the expansion of overheated material at near and above critical conditions at the top-level layer.[14] For higher fluences, both the top and lower part ablate from the substrate. We define the complete removal of Ru as *full-ablation*.

A selection of dark-field images of illuminated sites for each of the six Ru thicknesses is shown in Figs. 3(a)–3(f). The local fluence decreases as the distance from the illumination center increases. Since the full-ablation threshold fluence is exceeded in the middle of all spots shown in the images, all damage mechanisms are present. The right halves of the images have been overlayed with semi-ellipses that outline annular regions where nanovolcanoes (between blue and green ellipses), top-level ablation (between orange and green ellipses), and full-ablation (inside the green ellipse) are seen. The green semi-ellipses indicate the full-ablation edges. Within this region, there is no ruthenium left and the substrate is exposed, as seen by bright-field microscopy. For the 8 and 10 nm thick (nominal) layer, when moving closer to the green ellipse, the nanovolcanoes grow in size until practically all nanovolcano vents overlap, forming the full-ablation area. This is schematically drawn in Fig. 3(g).

Figures 4(a)–4(f) show SEM images for all Ru thicknesses similar to the dark-field ones as presented in Fig. 3. In the additional zoomed-in SEM images [Figs. 4(g)–4(r)], round dark shapes bordered by bright rims have emerged from the ruthenium layers. Since their sizes range from 50 to 500 nm, and because AFM images show that the rims are higher than the surrounding area, these structures resemble *nanovolcanoes*. Furthermore, the onset of

top-level ablation and full-ablation are shown by their respective edges. The yellow rectangles and arrows in Figs. 4(a)–4(f) indicate the locations of the zoomed-in SEM images.

For the 8 and 10 nm layers, nanovolcanoes start to form on the inside of the blue ellipses as indicated in Figs. 3(a) and 3(b). From here, they increase in number and size until the vents of the nanovolcanoes cover (almost) the entire area [Figs. 4(g), 4(m), 4(h), and 4(n)]. From here on, no ruthenium is left and full-ablation is reached. Figure 3(g) shows a schematic drawing of the nanovolcano formation over the ruthenium layer and its full-ablation.

For the 20, 25 and 40 nm thick (nominal) ruthenium layers, top-level ablation occurs [Figs. 4(j)–4(l)]. The corresponding top-level ablation edge is indicated by the orange semi-ellipses in the dark-field images [Figs. 3(d)–3(f)]. Between this edge and the full-ablation edge (green ellipses), the top layer of the ruthenium is missing. Here, only a few nanovolcanoes can be seen [Figs. 4(j)–4(l)], which are often positioned closer to the top-level ablation *edge* than the full-ablation edge [Figs. 4(p)–4(r)].

For a ruthenium nominal thickness of 15 nm, no top-level ablation has occurred [Fig. 4(i)]. However, a slightly elevated edge is observed and is positioned slightly outside the blue ellipses at the dark-field image in Fig. 3(c). Since such an elevation is not observed in the thinner layers, and top-level ablation is observed in the thicker ones, the 15 nm thick (nominal) layer seems to represent a transition layer thickness for the appearance of top-level ablation. Additionally, a fair number of nanovolcanoes are present around the elevation edge. However, the number of nanovolcanoes and sizes decrease when moving closer to the full-ablation border, which looks similar to that for thicker layers.

B. Threshold fluences and Liu-analysis

With dark-field microscopy, the outer edges of the areas A spanned by the identified damage mechanisms (see Fig. 4) were obtained. When a damage mechanism is bounded by a certain threshold fluence F_{th}, A and $\ln(F_0)$ should follow the linear relation $A = a\ln(F_0) + b$ [see also Eqs. (2) and (3)] for Gaussian beams with a peak fluence F_0.[21] In Fig. 5, the area A spanned by the outer edge of a damage mode vs $\ln(F_0)$, the so-called *Liu-plots*, are plotted for all six samples. The blue, orange, and green data points and their linear fits indicate nanovolcano formation, or top-level ablation, and the full-ablation respectively. The linear fits intersect the horizontal axis at $\ln(F_{th})$, where F_{th} is the corresponding fluence threshold of the corresponding damage mechanism [see Eq. (3)]. The fits are obtained by a recursive RANSAC approach.[24] Note that only the linear fits corresponding to nanovolcano formation (blue), top-level ablation (orange), full-ablation (green), and their corresponding data points are shown and are marked according to their color. In Fig. 7 of the supplementary material, this figure is shown including other damage mechanisms as well. At Fig. 5(a), the blue dashed line indicates that F_{NV}, the nanovolcano formation threshold fluence, is obtained by inspecting SEM images. SEM was used because of the low contrast of the nanovolcano formation onset in the dark-field images. Therefore, no nanovolcano formation edges were extracted from the dark-field images, and therefore, no blue data points are visible in Fig. 5(a). The top-level
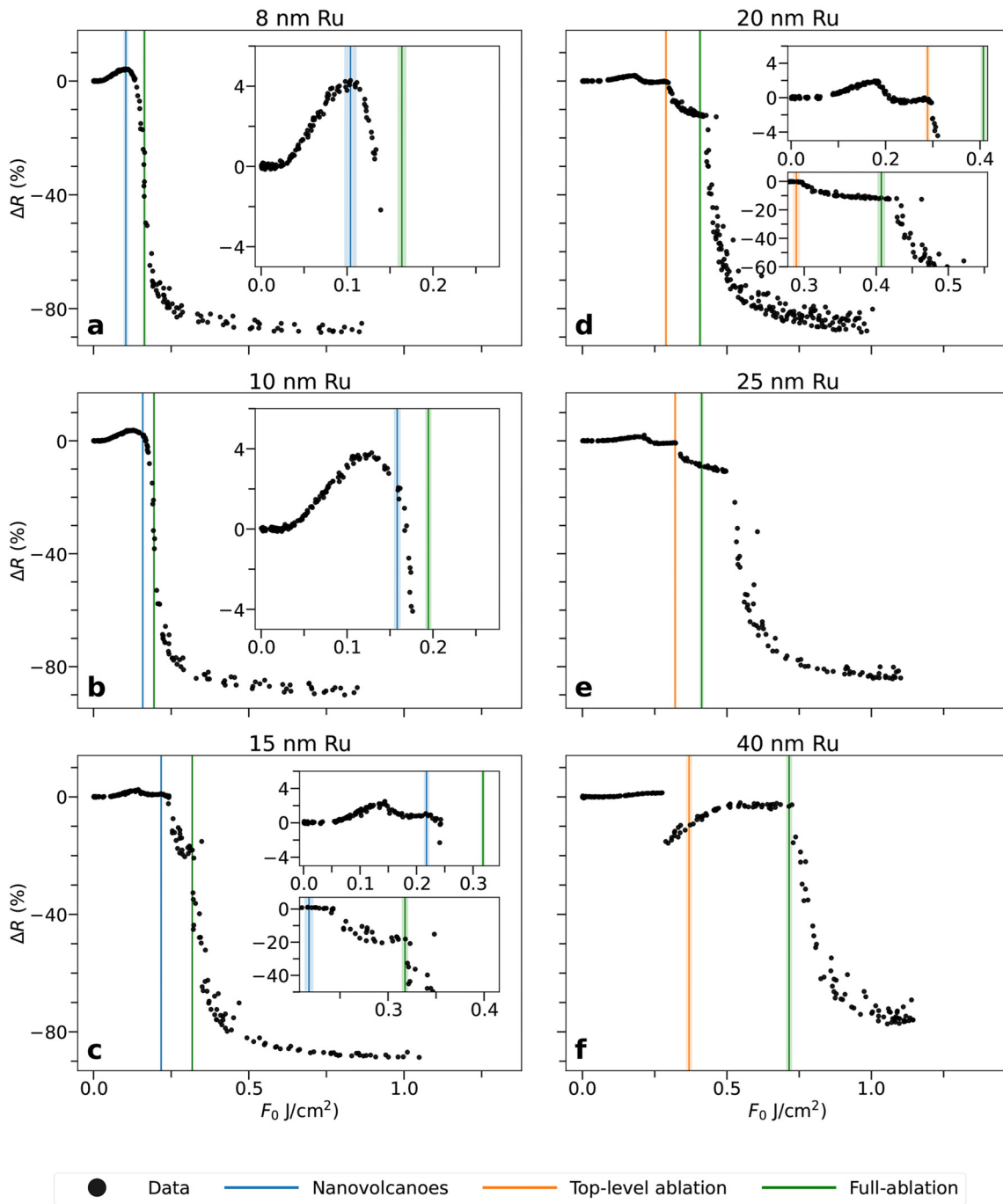
FIG. 2. Relative reflection change ΔR vs peak fluence F_0 for (nominal) 8, 10, 15, 20, 25, and 40 nm ruthenium on borosilicate glass substrates. Only the threshold fluences for three damage mechanisms, as identified by SEM, for each layer thickness are shown by the vertical lines. The blue vertical lines indicate the fluence threshold for nanovolcano formation in (a)–(c), and the orange lines in (d)–(f) indicate the top-level ablation threshold fluence. In all figures, the green lines mark the full-ablation threshold fluence. The corresponding uncertainty in these values is indicated by the lighter band around each vertical line, which is due to their small widths, only visible in the insets.
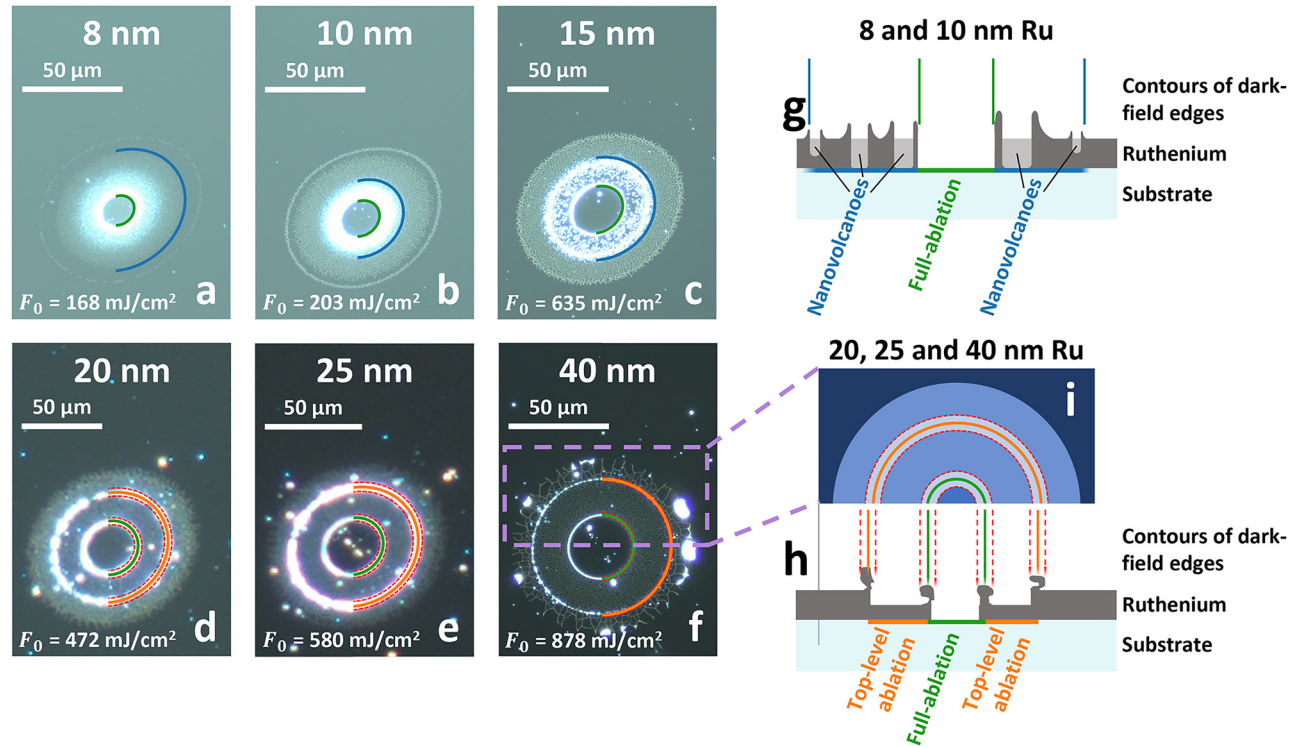
FIG. 3. (a)–(f) Dark-field microscopy pictures of single pump-shot illumination of 8, 10, 15, 20, 25 and 40 nm thick (nominal) ruthenium layers on borosilicate glass. At each picture, all damage mechanisms are present since the pump fluence is above the full-ablation thresholds ($F > F_{FA}$). Therefore, for all six layer thicknesses, the most inner damage edge is at a fluence level where full-ablation starts to occur (green). At the right half of each picture, semi-ellipses are drawn, indicating the onset of nanovolcano formation (blue), top-level ablation (orange), and full-ablation (green). In (d)–(f), each pair of neighboring dashed red contours is obtained from our analysis and corresponds to the inner and outer side of the white bright rim, which represents the top-level and full-ablation edges. The position of these respective ablation edges is defined to be in between each pair, as schematically shown in (i). Nanovolcanoes are found in the region between the blue and green ellipses, top-level ablation between the orange and green ellipses, and full-ablation inside the green ellipses. (g) and (h) Schematic drawings of the cross sections of 8 and 10 nm (g) and in 20, 25 and 40 nm (h) thick (nominal) ruthenium layers.

and full-ablation edges curl up as is visible in the SEM images Figs. 4(j)–4(l) and Figs. 4(o)–4(r) respectively. In the dark-field microscopy images, the entire curled up zone results in a bright annulus. Increasing the exposure time and brightness of the microscope light source can appear to widen this annulus even further. Each annulus has an inner and outer contour in the dark-field images as shown in Figs. 3(h) and 3(i). Therefore, pairs of the orange and/or green linear fits are shown in Figs. 5(d)–5(f), where each fitting pair represents the inner and outer contour of an annulus. We define the corresponding top-level or full-ablation threshold fluence (F_{th}) to lie exactly in the middle between the inner and outer contour. Therefore, F_{th} is obtained by averaging the fit parameters of the two corresponding fits. Here, $F_{th} \approx \exp(-(b_i + b_o)/(a_i + a_o))$, where a_i and a_o are the slopes and b_i and b_o the offsets of the Liu-fits corresponding to the inner and outer contour. The FWHM of the beam, d, is retrieved by using Eq. (3) with $a_{th} = \frac{1}{2}(a_i + a_o)$. Since these values for d are close to the measured ones, this suggests that the above assumption is valid.

All damage thresholds F_{th} for nanovolcano formation, top-level ablation, and full-ablation are indicated by the blue, orange, and green vertical lines in the ΔR vs F_0 plots of Fig. 2 as well. At every fairly abrupt change in the slope of ΔR in Fig. 2, a fluence threshold F_{th} was found (see Fig. 7 of the supplementary material). This is a further indication that such abrupt changes mark different damage mechanisms. The increased reflectivity, nanovolcano formation, top-level, and full-ablation will be discussed in further detail in Secs. III C and III D, whereas all other damage mechanisms are briefly described in Figs. 3 and 5 of the supplementary material only. Note that not all fluence thresholds have been obtained by Liu-analysis since not all damage mechanisms create a big enough contrast in the dark-field images. These additional thresholds are obtained by estimating the position of the damage edge from SEM images and subsequently calculating the local fluence at those borders based on the known beam profile. In Table II of the supplementary material, an overview of all obtained thresholds and damage mechanisms can be found, as well as their corresponding SEM images.
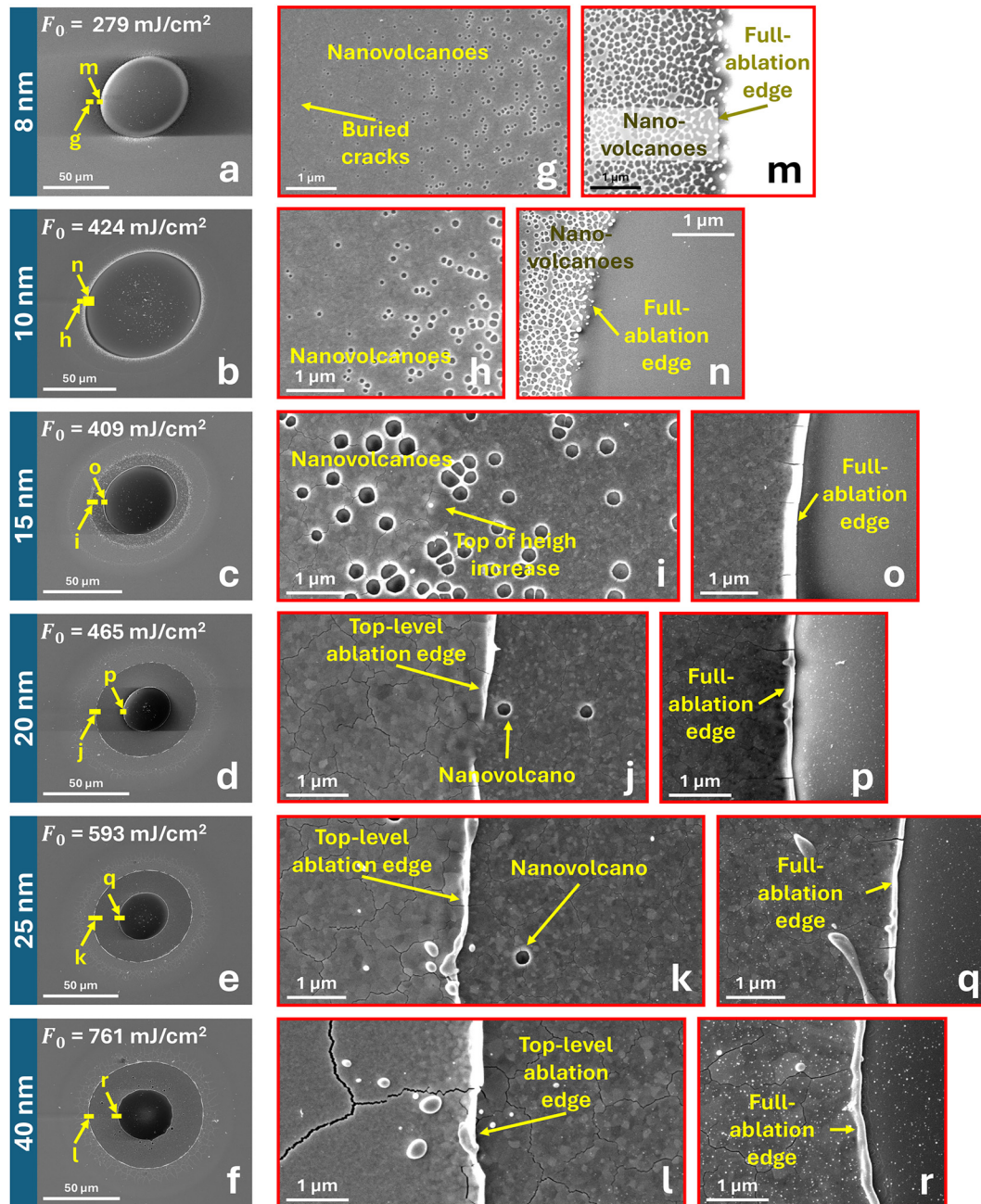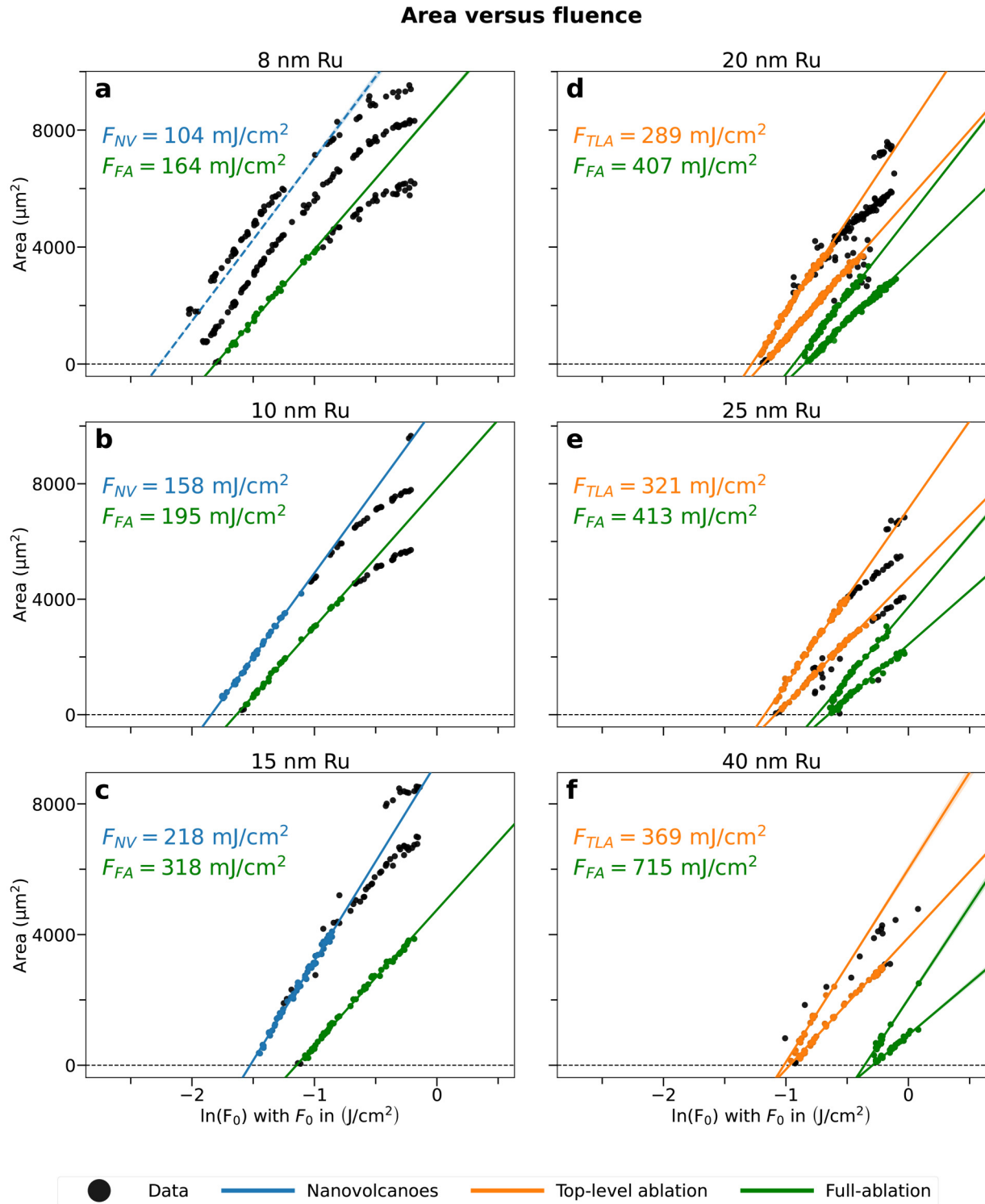
FIG. 4. SEM images of 8, 10, 15, 20, 25 and 40 nm thick (nominal) ruthenium layers on borosilicate glass illuminated above the full-ablation damage threshold. The arrows that point at the small yellow rectangles in (a)–(f) indicate the location of the zoomed-in images shown on the right (g)–(r). Nanovolcanoes and/or top-level ablation edges are shown in (g)–(n), whereas (m)–(r) are taken at the full-ablation edges.

C. Morphology

Figures 6(a) and 6(b) show optical dark-field microscopy and SEM images of a site on a 10 nm thick (nominal) ruthenium layer, illuminated just above the nanovolcano threshold fluence (F_{NV}).

Figures 6(a) and 6(b) are the dark-field and SEM overview images of the entire damaged site. Both show a bright center, which is the area where the nanovolcanoes are present. The red rectangle marks the position where the zoomed-in SEM and AFM images

Area versus fluence

FIG. 5. Liu-plots of single pulse laser damage experiments on 8, 10, 15, 20, 25 and 40 nm thick (nominal) ruthenium layers on borosilicate glass, obtained by inspecting dark-field images. Blue, orange, and green linear fits are shown corresponding to the onset of nanovolcano (NV), top-level (TLA), and full-ablation (FA) respectively.
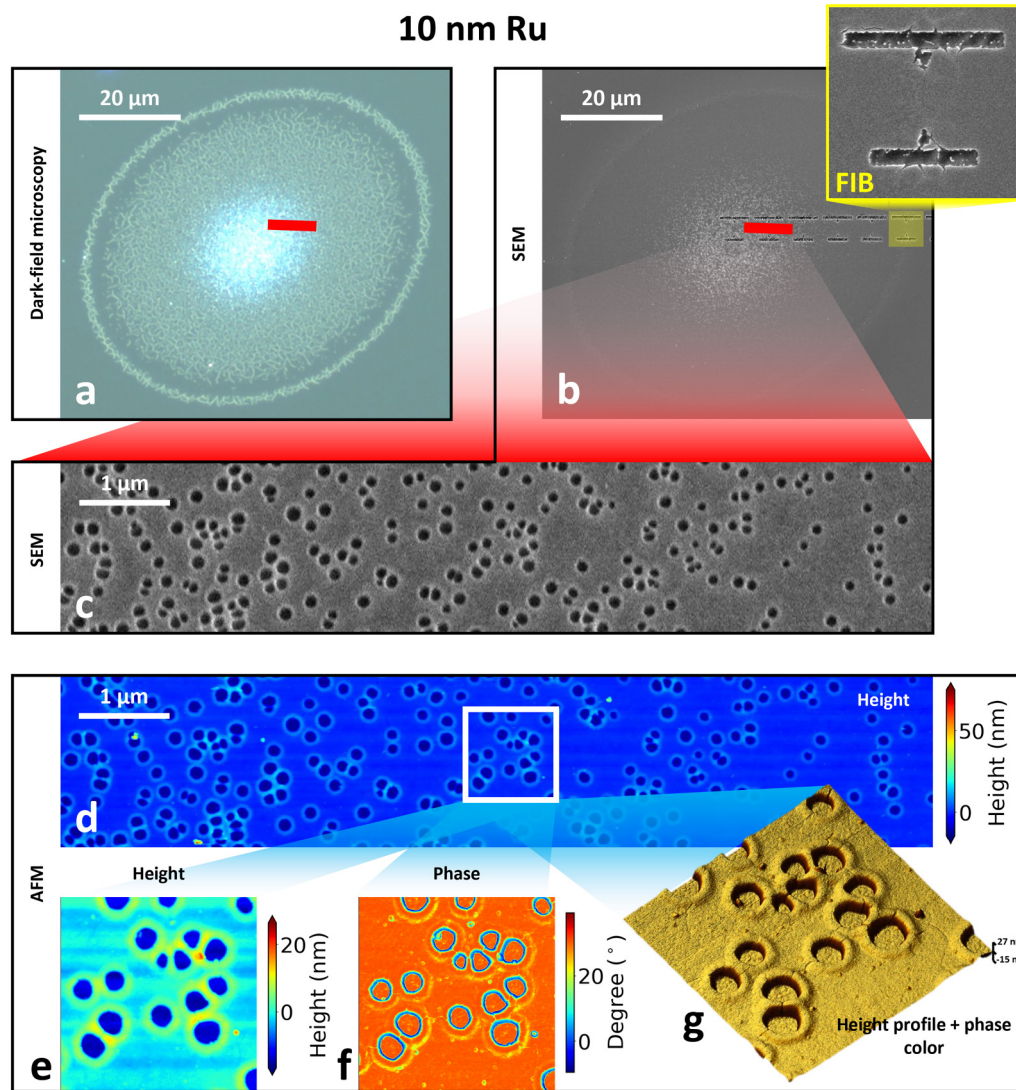
FIG. 6. (a) Dark-field microscopy images of a single damaged site on a 10 nm Ru film on borosilicate glass. The site was illuminated with a single pulse with a fluence above the nanovolcano formation threshold (F_{NV}). (b) SEM image of the whole damaged site. After laser exposure, markers have been made in the ruthenium layer by a focused ion beam (FIB) to help find locations on the damaged spot to be imaged using an AFM. The inset of (b) shows one set of FIB markers composed of two lines and two (very small) triangles. In total, six of those FIB marker sets, that are positioned next to each other, are shown in (b). Both (a) and (b) show a bright center, the area where the nanovolcanoes have formed. The red rectangle marks the position of the zoomed-in SEM and AFM images [(c) and (d)]. (e) and (f) are the height and phase profiles of the area marked by the white rectangle, and (g) shows the 3D height profile overlayed with the phase.

[Figs. 6(c) and 6(d)] were taken. Here, each nanovolcano can be identified by its round center (vent) and by the rim. These are indicated by the dark and bright color respectively in SEM, and by their height in the AFM height profile. The vent diameter varies between ≈60 and 160 nm here. Figures 6(e)–6(g) are the height and phase profiles of the area marked by the white rectangle in Fig. 6(d). In the SEM image, the volcanoes are evident as dark circular features in the ruthenium layer. In the nanovolcano *vents*, the AFM image shows a negative height indicating that

material is indeed missing. These vents are bordered by a few nanometers higher rim, and in most cases, the substrate in the vents is exposed.

In Figs. 7(a) and 7(b), the height and phase profile of a single nanovolcano obtained by AFM are shown. Here, a dashed line indicates where the height and phase cross sections are taken, that are plotted in Figs. 7(c) and 7(d). Around each nanovolcano vent, a higher *rim* is formed. For fluences between F_{NV} and a bit below F_{FA}, the missing volume of the vent corresponds to the volume of
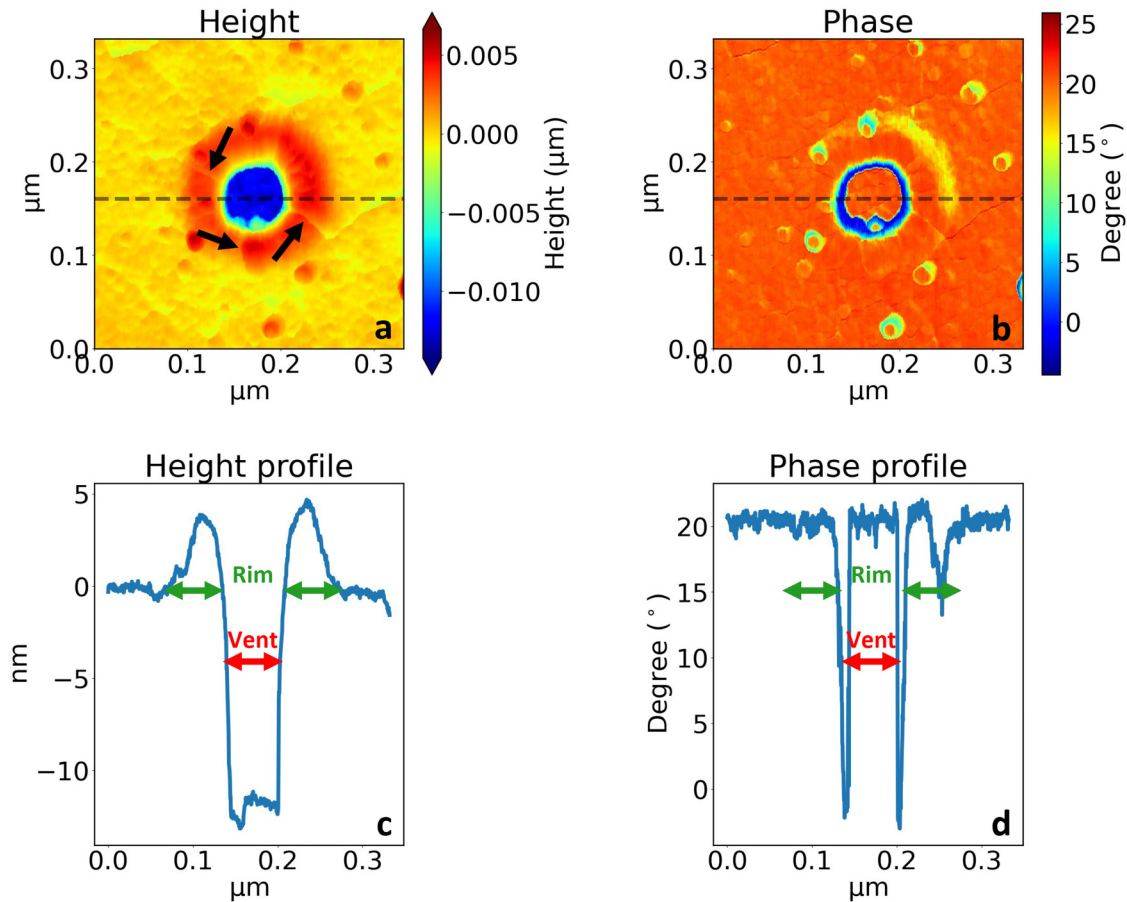
FIG. 7. High-resolution AFM height (a) and phase profile (b) scan of a single nanovolcano. (c) and (d) correspond to cross sections along the horizontal dashed lines visible in (a) and (b). Around each nanovolcano vent, a higher rim is formed. A crack also runs through the volcano but this is difficult to see due to the limited AFM spatial resolution. The black arrows in (a) point at the parts of the crack that run through the volcano rim (see also the SEM images in Fig. 4 of the supplementary material). The nanovolcano is at the same illuminated site as presented in Fig. 6, but positioned approximately 7 μm to the right of Figs. 6(e)–6(g), at a position where the fluence is lower.

the rim, indicating that no material is missing. However, for nano-volcanoes with a local fluence relatively close to the full-ablation threshold, up to ≈35% less material is present. This means that already some material is ablated before reaching the full-ablation threshold fluence F_{FA} (see Sec. V of the supplementary material). Note that Fig. 7(c) is a cross section of a nanovolcano, at which the rim and vent area are visible. These areas are not equal, but their volumes are approximately equal. This is because the rim is positioned further away from the center of the nanovolcano and, therefore, has a larger circumference than the vent.

In the vents, the bottom is relatively flat [see Fig. 7(c)] and is of the same depth as the other nanovolcanoes in the same Ru layer. Additionally, when the AFM tip reaches the bottom, there is a big neg-ative jump in the phase signal as can be seen in Figs. 7(b) and 7(d). The flatness and alignment of the vent bottoms combined with the observed big phase jumps suggest that the glass substrate is exposed.

An EDX scan covering multiple nanovolcanoes, shown in Fig. 8, further demonstrates that there is no significant amount of ruthe-nium present in the nanovolcano vents. We note that SEM images (see Fig. 4 of the supplementary material) show that crack lines seem to run through all nanovolcanoes. Additionally, as is visible in the SEM image of Fig. 6(c), the nanovolcanoes are not evenly distributed, but seem to be grouped along lines. However, this is only clearly visible in SEM images with a higher spatial resolution in which it can be seen that these ragged lines correspond to cracks that run along the ruthenium surface. These cracks already form at lower local fluences, whereas nanovolcanoes start to form at higher fluences. This suggests that, for increasing fluence, cracks form first, followed by nanovolcanoes which form along those crack lines. We note that in Fig. 7(a), a crack also runs through the volcano but this is difficult to see due to the limited AFM spatial resolution.
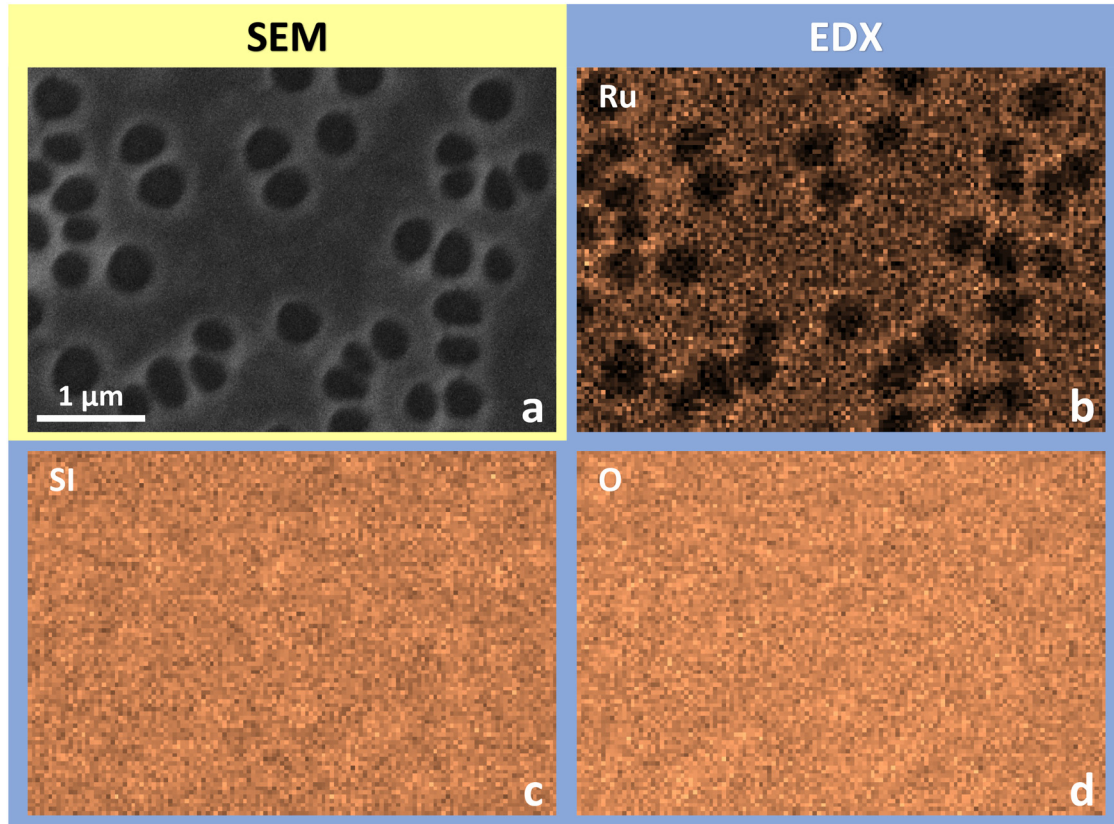
FIG. 8. (a) SEM image of part of an illuminated site on a nominally 10 nm thick ruthenium layer on borosilicate glass. (b)–(d) are the corresponding EDX maps of Ru, Si and O respectively, where the scaling of the colormap is optimized per element. Note the near absence of Ru in the volcano vents. Although difficult to see, in the vents, the Si and O signals are slightly higher, which is due to the direct probing of the substrate. Elsewhere, the signal is partly blocked by the Ru layer.

D. Optical changes and formation mechanism

As demonstrated by the *in situ* probe measurements (Fig. 2) of the sites illuminated with a single laser-shot, the first change in the reflected signal is a small increase in reflectivity at relatively low fluences. The onset of this reflectivity increase lies at a fluence level where neither nanovolcano formation nor top-level ablation have yet occurred. Both these damage mechanisms are first observed at significantly higher fluences than the fluence where the reflectivity increase occurs. Neither mechanism can therefore be directly responsible for the observed reflectivity increase. However, there are additional arguments why nanovolcano formation and top-level ablation cannot explain the subtle reflectivity changes observed at low fluences. Nanovolcanoes, as seen by the dark-field images in Fig. 3, clearly scatter light in all directions. This would lower the amount of specularly reflected light rather than increase it. For top-level ablation, a significant top part of the ruthenium layer has been removed. Optical multilayer calculations, using the transfer matrix method,[25] of Ru on glass show that this thinning of the layer would lead to a *decrease* of the optical reflectivity (see Fig. 8 of the supplementary material).

To learn more about the possible causes of the small reflectivity increase, we have also performed Electron Backscatter Diffraction (EBSD) to measure the crystallinity of the Ru layers after exposure to a single laser pulse. Since our Ru layers are polycrystalline, EBSD allows us to obtain grain size and orientation at various locations within an illuminated spot. Figure 9(a) shows a dark-field image of a single-shot illuminated site on a 8 nm thick (nominal) layer of ruthenium. Here, the red rectangles mark the locations of the obtained EBSD-scans as shown in Figs. 9(c)–9(g), and Fig. 9(b) is a scan of a pristine site used as a reference. The local fluences of each EBSD-map are in the $\Delta R > 0$ regime but below the nanovolcano formation threshold. From Figs. 9(d)–9(g), it is clear that for $F_{local} > 77 \, \text{mJ/cm}^2$, the grain size increases with respect to the pristine material [Fig. 9(b)]. Note that a light ring is visible in the dark-field image. Here, a band with relatively big grains with a (0001) Ru-structure can be found, which may contribute to a positive ΔR. However, its formation mechanism is currently unknown. Since the grain size of the pristine ruthenium is smaller than our spatial resolution, individual grains on Figs. 9(b) and 9(c) and the right side of Fig. 9(g) cannot be resolved. At the
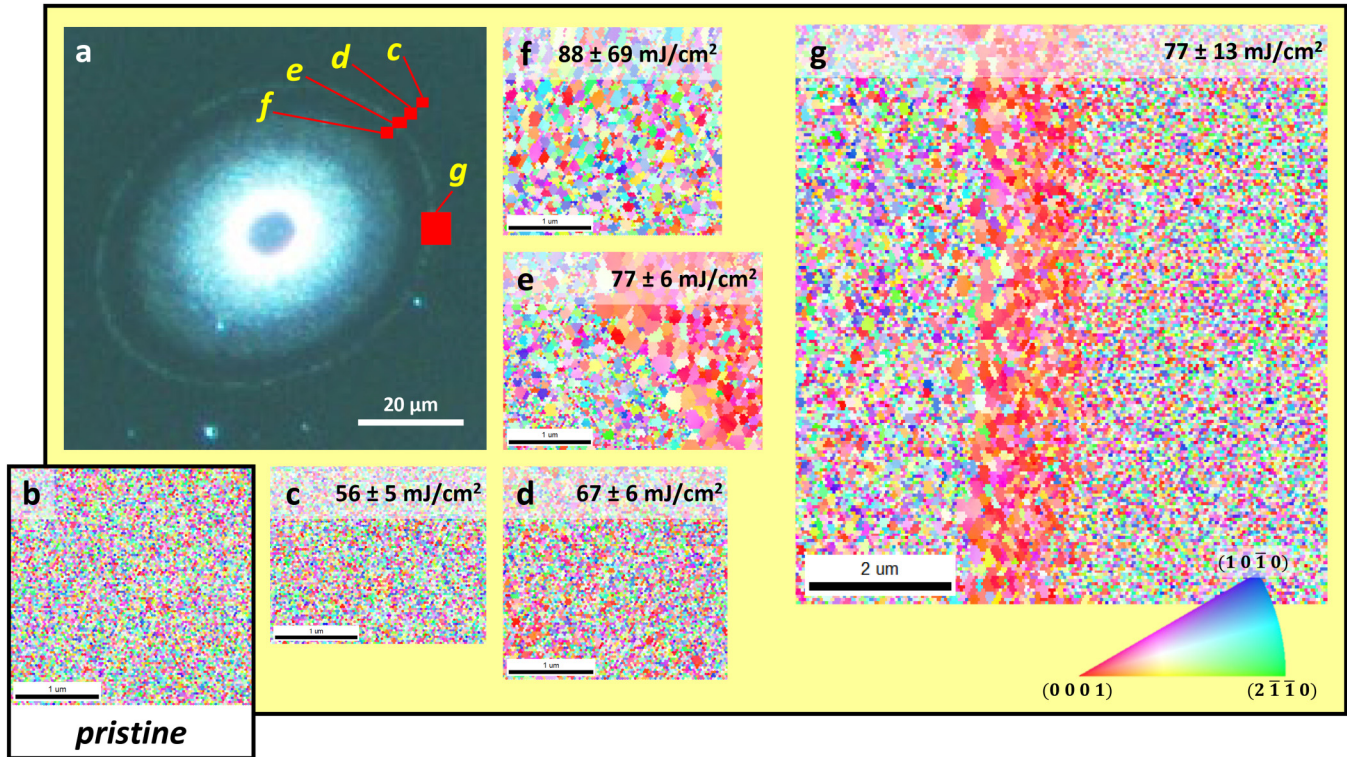
FIG. 9. (a) Dark-field microscopy image of a single-shot-illuminated site of an 8 nm thick layer of ruthenium on borosilicate glass. The red rectangles indicate the locations of the EBSD-maps [(c)–(f)]. Here, the local fluences are below the threshold fluence for nanovolcano formation ($F_{local} < 104 \, \text{mJ/cm}^2$) in the fluence regime, where $\Delta R > 0$. The average values for F_{local} of each map are indicated at the corresponding EBSD image. The inverse polar figure maps show the crystal direction, which is the direction normal to the sample. Each color corresponds to the direction in the range between (0001), (10$\bar{1}$0), and (2$\bar{1}\bar{1}$0) according to the triangle legend in the bottom right of the figure.

fluence level that corresponds to scan Fig. 9(c) however, $\Delta R > 0$, so it is very likely that the grain size increased here too, however not exceeding our spatial resolution ($\approx$30 nm). For recrystallization to take place, the ruthenium has had to reach the melting temperature ($T_m = 2606 \, \text{K}$ at atmospheric pressure) first. Additional two-temperature model (TTM) calculations are performed to obtain F_m, the fluences for which T_m is reached (see Fig. 6 of the supplementary material). Here, F_m is lower than fluences for which nanovolcano formation and top-level ablation occurs, which indicates that recrystallization takes place after reaching the melting threshold. Increasing the grain size leads to a bigger mean free path of the electrons oscillating in response to the electric field of the probe, which will decrease the resistivity of our ruthenium layer and increase reflectivity.[15,26,27] Therefore, it is highly probable that the nano-structural change in grain size is directly responsible for the small reflection increase we observe in the measurements. Interestingly, this is similar to what we observed recently for aluminum, although for Ru, the pristine grain size is considerably smaller. In some places nanovolcanoes form, indicating that Ru has flowed creating a rim. These volcanoes are surrounded by topographically flat molten and subsequently recrystallized ruthenium.

The question remains what physical mechanism causes the formation of nanovolcanoes and top-level ablation. In Ref. 14, it was reported that, at high fluences, fast energy deposition in a sub-surface layer leads to *two-level ablation*. Here, the top-layer is ablated as a gas–liquid mixture, whereas the bottom-layer is ablated via a cavitation process. However, for somewhat lower fluences, only the top-layer is ablated (top-level ablation), whereas the bottom-layer is still present on the surface. Therefore, the structure of this bottom-layer may have been changed perhaps giving rise to the formation of frozen cavities as reported in Ref. 14. Our measurements show that top-level ablation occurs in ruthenium layers of $\approx$20 nm and thicker, which is accompanied with a fairly low number of isolated nanovolcanoes. However, for thinner layers, there is no top-level ablation and instead, nanovolcano formation is prevalent. For the 8 and 10 nm layers, the nanovolcano number density and size increase for higher local fluence. Here, the nano-scale morphology of the substrate may play a role. Some evidence for this is obtained by illuminating a 8 nm ruthenium layer deposited on a borosilicate glass substrate that was lightly scratched with sanding paper, before cleaning the substrate in a sonic bath and base piranha solution. After deposition of the Ru, the scratch lines
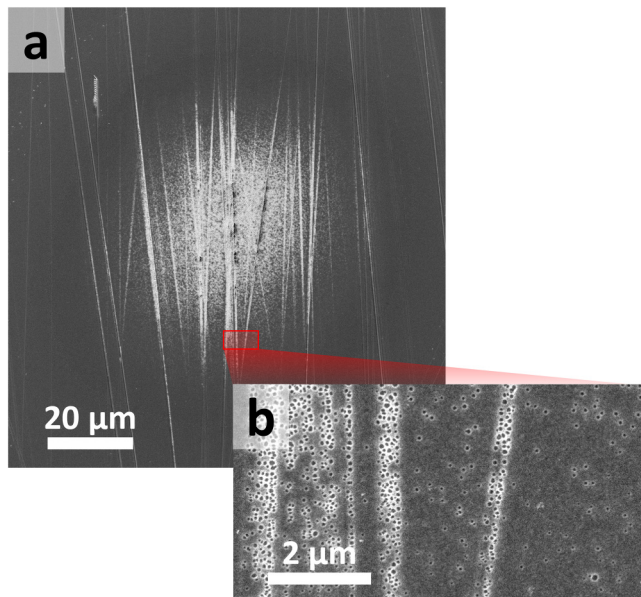
FIG. 10. SEM images of a site on an 8 nm (nominal) thick Ru layer deposited on a 0.5 mm thick scratched borosilicate glass substrate, and illuminated with a single pump pulse. The substrate is scratched by sanding paper and cleaned in a sonic bath and a base piranha solution before ruthenium deposition. Nanovolcanoes form predominantly along the scratch lines as is shown by the bright lines in the SEM image in (a) and from the zoomed-in section shown in (b).

are visible by SEM as is shown in Fig. 10. Here, the SEM images clearly show that the nanovolcanoes tend to grow along those lines. This suggests that the roughness facilitates their formation, perhaps by increasing the local optical near-field, enhancing the probability of their formation at these locations.

In view of the use case scenarios for metrology applications related to wafer alignment, any form of light-induced material change has to be avoided. We found that this happens to be the fluence for which the smallest measurable increase in reflectivity occurs in response to a pump laser pulse. Theses fluences are summarized in Table II for the different Ru layer thicknesses.

TABLE II. Overview of the threshold fluences at the smallest measurable increase in reflectivity.

Thickness (nm)		
Nominal	Measured	F_{th} (mJ/cm^2)
8	9.2	23 ± 10
10	11.6	62 ± 30
15	17.2	28 ± 15
20	23.0	66 ± 30
25	28.8	54 ± 40
40	45.9	93 ± 30

IV. CONCLUSION AND SUMMARY

We studied optical changes in 8 to 40 nm thick ruthenium films on various substrates induced by a single ultrafast laser pulse. For fluences below the full-ablation damage thresholds, for all Ru nominal thicknesses we studied, the reflectivity initially increases by a few percent. We have determined the damage threshold fluence at which the smallest measurable material change occurs (Table II). When the fluence increases further, the reflectivity shows fairly abrupt changes for samples with nominal layer thicknesses of 15 nm and higher. Additionally, at fluences below full-level ablation, different morphological changes such as nanovolcano formation and top-level ablation are observed. The nanovolcanoes appear to have been formed by molten Ru that has locally been pushed outward and has flowed over the surrounding area. Furthermore, nanovolcanoes appear to be positioned on crack lines in the Ru. In top-level ablation, only the top part of the ruthenium layer is ablated whereas the lower part still remains on the substrate, which occurs in ruthenium layers of 20 nm thickness (nominal) and more. Here, a concentration of nanovolcanoes is located around the top-level ablation edge.

Neither top-level ablation nor nanovolcano formation can explain the small increase in reflectivity at low fluences directly. Instead, using Electron Backscatter Diffraction, we find that Ru grains have melted and resolidified into bigger ones, most likely giving rise to the small increase in reflectivity by the accompanying increase in the mean free path of the electrons. This is similar to what was observed for thin Al films[15] and suggests that there may be more metals for which this occurs. For optical metrology in semiconductor device manufacturing, subtle light-induced changes in the reflectivity, due to changes in conductivity and morphology, may serve as early warning signals to prevent catastrophic damage. Particularly in ruthenium, the good nanoscale electrical conductivity may be influenced by the light-induced grain size change. Therefore, at low fluence regimes, where small optical changes occur well below any catastrophic damage, the functionality of semiconductor devices may already be affected.

AUTHOR DECLARATIONS
Conflict of Interest

The authors have no conflicts to disclose.

17 January 2025 09:41:12

Author Contributions

Ester Abram: Conceptualization (equal); Data curation (lead); Formal analysis (lead); Investigation (lead); Methodology (equal); Software (equal); Writing – original draft (equal); Writing – review & editing (equal). **Nikolai Orlov:** Data curation (supporting); Formal analysis (supporting); Investigation (supporting); Writing – original draft (equal); Writing – review & editing (equal). **Erik C. Garnett:** Supervision (equal); Writing – original draft (supporting); Writing – review & editing (supporting). **Paul Planken:** Conceptualization (equal); Formal analysis (equal); Funding acquisition (lead); Investigation (equal); Methodology (equal); Supervision (lead); Writing – original draft (equal); Writing – review & editing (equal).

DATA AVAILABILITY

The data that support the findings of this study are available from the corresponding author upon reasonable request.

REFERENCES

[1] G. Zhang, M. Graef, and F. van Roosmalen, in *56th Electronic Components and Technology Conference 2006* (IEEE, 2006), pp. 151–157.

[2] M. M. Waldrop, Nat. News **530**, 144 (2016).

[3] W. Steinhögl, G. Schindler, G. Steinlesberger, M. Traving, and M. Engelhardt, J. Appl. Phys. **97**, 023706 (2004).

[4] D. Josell, S. H. Brongersma, and Z. Tőkei, Annu. Rev. Mater. Res. **39**, 231 (2009).

[5] D. Choi and K. Barmak, Electron. Mater. Lett. **13**, 449 (2017).

[6] T. M. Philip, N. A. Lanzillo, T. Gunst, T. Markussen, S. Cobb, S. Aboud, and R. R. Robison, Phys. Rev. Appl. **13**, 044045 (2020).

[7] E. Milosevic, S. Kerdsongpanya, A. Zangiabadi, K. Barmak, K. R. Coffey, and D. Gall, J. Appl. Phys. **124**, 165105 (2018).

[8] C. Messinis, T. T. M. van Schaijk, N. Pandey, A. Koolen, I. Shlesinger, X. Liu, S. Witte, J. F. de Boer, and A. den Boef, Opt. Express **29**, 38237 (2021).

[9] T. van Gardingen-Cromwijk, S. Konijnenberg, W. Coene, M. Adhikary, T. Tukker, S. Witte, J. F. de Boer, and A. den Boef, Light Adv. Manuf. **4**, 453 (2023).

[10] I. A. Makhotkin, I. Milov, J. Chalupský, K. Tiedtke, H. Enkisch, G. de Vries, F. Scholze, F. Siewert, J. M. Sturm, K. V. Nikolaev, R. W. E. van de Kruijs, M. A. Smithers, H. A. G. M. van Wolferen, E. G. Keim, E. Louis, I. Jacyna, M. Jurek, D. Klinger, J. B. Pelka, L. Juha, V. Hájková, V. Vozda, T. Burian, K. Saksl, B. Faatz, B. Keitel, E. Plönjes, S. Schreiber, S. Toleikis, R. Loch, M. Hermann, S. Strobel, R. Donker, T. Mey, and R. Sobierajski, J. Opt. Soc. Am. B **35**, 2799 (2018).

[11] I. Milov, V. Lipp, D. Ilnitsky, N. Medvedev, K. Migdal, V. Zhakhovsky, V. Khokhlov, Y. Petrov, N. Inogamov, S. Semin, A. Kimel, B. Ziaja, I. Makhotkin, E. Louis, and F. Bijkerk, Appl. Surf. Sci. **501**, 143973 (2020).

[12] F. Akhmetov, I. Milov, S. Semin, F. Formisano, N. Medvedev, J. M. Sturm, V. V. Zhakhovsky, I. A. Makhotkin, A. Kimel, and M. Ackermann, Vacuum **212**, 112045 (2023).

[13] S. Bucklow, Stud. Conserv. **42**, 129 (1997).

[14] I. Milov, V. Zhakhovsky, D. Ilnitsky, K. Migdal, V. Khokhlov, Y. Petrov, N. Inogamov, V. Lipp, N. Medvedev, B. Ziaja, V. Medvedev, I. Makhotkin, E. Louis, and F. Bijkerk, Appl. Surf. Sci. **528**, 146952 (2020).

[15] E. Abram, I. Milov, N. Orlov, K. van Druten, E. C. Garnett, and P. Planken, Opt. Express **32**, 4564 (2024).

[16] Epredia Inc., *Microscope Slides and Coverslips* (Epredia Inc., 2021).

[17] E. D. Palik, *Handbook of Optical Constants of Solids* (Academic Press, 1998), Vol. 3.

[18] W. M. Haynes, *CRC Handbook of Chemistry and Physics*, 95th ed. (CRC Press, 2014).

[19] L. Ackermann, C. Roider, K. Cvecek, and M. Schmidt, Appl. Phys. A **128**, 877 (2022).

[20] F. Brandi, N. Burdet, R. Carzino, and A. Diaspro, Opt. Express **18**, 23488 (2010).

[21] J. M. Liu, Opt. Lett. **7**, 196 (1982).

[22] E. Abram, I. Milov, N. Orlov, N. van Druten, E. C. Garnett, and P. Planken, Opt. Express **32**, 2–3 (2024).

[23] The reported thicknesses throughout the paper are the aimed nominal thicknesses. The inferred thickness from ellipsometry are ≈15% higher than the nominal ones and are obtained from ellipsometry measurements where a native oxide of 0.5 nm is assumed. Both the nominal and inferred thicknesses can be found in Table 1 in the supplementary material. Note that the inferred thicknesses are used for the calculations.

[24] M. A. Fischler and R. C. Bolles, Commun. ACM **24**, 381–395 (1981).

[25] S. J. Byrnes, "Multilayer optical calculations," arXiv:1603.02720 (2020).

[26] P. Schmitt, S. Stempfhuber, N. Felde, A. V. Szeghalmi, N. Kaiser, A. Tünnermann, and S. Schwinde, Opt. Express **29**, 19472 (2021).

[27] T. T. Hu, J. H. Hsu, J. C. Huang, S. Y. Kuan, C. J. Lee, and T. G. Nieh, Appl. Phys. Lett. **101**, 011902 (2012).